Available online at www.sciencedirect.com
SCIENCE DIRECT®
ELSEVIER
International Journal of Solids and Structures 43 (2006) 4008–4027
INTERNATIONAL JOURNAL OF SOLIDS and STRUCTURES
www.elsevier.com/locate/ijsolstr

Finite element analysis of post-buckling dynamics in plates. Part II: A non-stationary analysis

Hui Chen, Lawrence N. Virgin *

Pratt School of Engineering, Duke University, Durham, NC 27708-0300, United States

Received 7 April 2005
Available online 24 June 2005

Abstract

With the secondary bifurcation and the local post-secondary buckling behavior being analyzed in Part I, Part II of this study consists of developing an adaptive non-stationary load sweeping algorithm to investigate post-buckling dynamics and mode jumping phenomena of generally (mechanically and thermally) loaded thin plates in a global context. The non-stationary sweeping procedure has the merits of adapting large load steps to capture static characteristics of stable equilibrium paths both before and after mode jumping and reduce automatically the step size to ensure a dynamic transition between the two stable branches. Thus, it is computationally effective. Furthermore, by adopting the non-stationary sweeping scheme, this procedure can avoid spurious convergence of the transient response to an unstable equilibrium.

Corresponding to different post-secondary bifurcation forms, which are determined using asymptotical finite element analysis developed in Part I, subsequent buckling patterns of various complexity occurring after mode jumping are obtained using the method developed in this article. Qualitative changes in post-buckled patterns are observed after the occurrence of the secondary bifurcation or the mode jumping. Free vibration analysis using the tangent stiffness matrix obtained from the converged static or dynamic solutions shows a vibration modal shifting phenomena occurs during the process of the load sweep. The spurious convergence phenomenon caused by the application of the traditional hybrid static–dynamic method is found and explained.

Keywords: Finite elements; Bifurcation; Frequencies; Mode jumping

* Corresponding author. Tel.: +1 919 660 5342; fax: +1 919 660 8963.
E-mail address: l.virgin@duke.edu (L.N. Virgin).

0020-7683/$ - see front matter © 2005 Elsevier Ltd. All rights reserved.
doi:10.1016/j.ijsolstr.2005.04.037

1. Introduction

Compressively stressed elastic thin plates or panels may exhibit a complicated evolution of their post-buckled patterns. When loaded into the post-buckling regime, some structures may experience a sudden (dynamic) change of their buckling mode shapes, a phenomenon called mode jumping. Qualitatively different propagations of the post-buckling patterns have been observed in a series of experiments on uniaxially compressed plates or panels. In Stein's experiment (Stein, 1959; Stoll and Olson, 1997), mode jumping was observed when an aluminum plate (with unloaded edges free to move in-plane but constrained to remain straight) encountered a secondary instability, whereas no dramatic changes of the post-buckled patterns was found when a stiffened graphite panel (with free unloaded edges) was increasingly compressed to pass its secondary buckling load until the failure of the structure (Knight and Starnes, 1988). More experimental examples on mode jumping were reported in uniaxially compressions of a bilaterally constrained plate (Chai, 2002) and a four-edge integrated hat-stiffened composite panel (Falzon and Steven, 1997). For the former, a contact/buckling problem, the lateral constraints led to a sequential plate snapping process arising from the secondary buckling of contact zones in the plate, while for the latter the structure experienced smooth evolution of post-buckled patterns until the tertiary bifurcation point was reached, where the panel exhibited a dramatic change in buckling mode shapes. A detailed review of numerous analytical/numerical studies of mode jumping can be found in the references Chen (2004) and Chen and Virgin (in press).

The qualitatively different development of the buckling patterns can be partly explained by the local post-buckling analysis at the secondary (and higher order) bifurcation point(s). Asymptotic finite element analysis in Part I of the current study shows that the different combination of boundary conditions and load types may result in different post-secondary bifurcation forms (Chen and Virgin, in press). At the secondary bifurcation point, if the bifurcation type is determined as of subcritical (meaning that all the local post-secondary paths are unstable) mode jumping occurs immediately and a dramatic change of the post-buckled deformation shape can be observed. On the other hand, if an asymmetric or supercritical bifurcation type is encountered, the transition of the post-buckled pattern is smooth and mode jumping may be deferred to a tertiary or later bifurcation point. However, because mode jumping is characterized by the dynamic switch between two (disconnected) stable branches, the local perturbation approach often fails to predict the remote stable equilibrium state.

While the mode jumping of uniaxially compressed plates often indicates an increase of buckling wave number, more geometrically complicated post-buckled patterns have been observed in thermally loaded plates after the occurrence of mode jumping. This is because the latter demonstrates much stronger geometric non-linearity than the former (Chen and Virgin, 2004). In a recent experiment on the growth of a heteroepitaxial microelectronic film on a mismatched substrate, a complicated wrinkling pattern with in-plane anti-symmetric property was observed by Hobart et al. during the annealing of the thin film at a high temperature (Hobart et al., 2000). Although many physical insights of the wrinkling process have been revealed using various analytic methods (Sridhar et al., 2001, 2003; Huang and Suo, 2002; Palasantzas and De Hosson, 2003), these methods failed to explain the occurrence of the real anti-symmetric post-buckled pattern. This may be attributed to the fact that the above methods are limited to linear analysis approaches and that the film is assumed to be subjected to uniaxially compressive loading, ignoring the in-plane constraint on the unloaded edges. In addition, the plate model is considered as infinitely large with no boundary effects being taken into account, although many studies show that both in-plane and out-of-plane boundary constraints strongly affect the post-buckling behavior as well as mode jumping of the plate, see for example (Supple, 1968; Stoll, 1994; Everall and Hunt, 1999; Tiwari and Hyer, 2002).

Clearly, a complete analysis of the post-buckling behavior (including the mode jumping) of plate under general (mechanical and thermal) loading involves both the local post-secondary bifurcation analysis and a global procedure to capture the remote stable equilibrium branch to which the plate may jump. Full non-linear finite element analysis methods are usually used to achieve this goal. However, because of the disconnection of two

stable equilibrium paths, the standard quasi-static continuation method is not sufficient by itself to obtain the desired response of the structure. Many solution schemes has been developed to overcome this difficulty.

One scheme is to use a guessed solution which is assumed away from the primary post-buckling path as a starting computational point for the jumped branch; after the convergence of this trial solution is reached, a standard path-following method is continued to follow the post-jumped path (Marcinowski, 1999; Tiwari and Hyer, 2002). Obviously this strategy is not robust and some a priori information of the target branch is needed.

Another is the well-known hybrid static–dynamic method developed by Riks et al. (1996). In this strategy the standard quasi-static continuation method is used to follow the stable primary post-buckling path until the secondary bifurcation point is encountered, then a step load increment is applied and the response of the structure is sought dynamically; after the dynamical solution is converged near a remote stable solution (because of the structural damping) the quasi-static solution procedure is adopted again. Although this technique has been used successfully to solve various problems, for example, the damage of a compressed sandwich panel (Riks and Rankin, 2002) and the mode jumping of a compressed isogrid structure (Muheim and Johnson, 2003), for a thermally loaded structure, where the external force cannot be given explicitly, it may converge to an unstable solution. This spurious convergence phenomenon will be explained later in this paper. In addition, the application of this method needs manual intervention.

Other solution algorithms (e.g. the continuation-unsymmetrical Lanczos algorithm (Chien et al., 2000) and Newton–GMRES approach (Dossou and Pierre, 2003)) have also been proposed to solve the discrete von Kármán equation directly. However, in these approaches, the definition of mode jumping is somewhat different from what we adopt here: it is defined as the direct connection of the two stable solutions by an unstable one. When the problem becomes more complicated, such as in the thermal case, multiple unstable solution branches are required to connect these primary and target stable branches (Chen and Virgin, 2004). Clearly, using these path-following approaches to detect unstable connecting branches for a high dimensional non-linear system is unrealistic in our context. Besides, from the engineering point of view, we are primarily concerned with the stable solutions.

Based upon the local post-secondary analysis in Part I, in this paper an effective non-stationary load sweep algorithm is developed to investigate the post-buckling dynamics and the mode jumping phenomenon of the plate in a global context. The spurious convergence phenomenon caused by the classical hybrid static–dynamic approach is found and explained. A complete numerical analysis of the important characteristics of the mode jumping: the secondary bifurcation type, the morphological mutation of the buckled patterns, and the change of natural frequencies versus load is presented.

2. Non-stationary sweep algorithm

2.1. Method selection and spurious convergence

The mode jumping phenomenon is characterized by a dynamic snap from the current stable equilibrium position to a remote stable one when the load passes beyond the secondary critical point and the current equilibrium path becomes unstable. Typically, this phenomenon can be investigated either by using an entire transient analysis approach or a so-called hybrid static–dynamic method developed by Riks et al. (1996). Because of its computational efficiency the latter is widely used.

However, our numerical experiments (using the Hilbert–Hughes–Taylor α method) show that although the Riks' approach always succeeds in finding remote stable solutions for mechanically loaded plates, it often failed, even for very small time steps and kinetic energy thresholds, for the thermally loaded cases—the dynamic solution seems to converge to an unstable equilibrium position near the secondary bifurcation point. A similar example can be found in the analysis of a simple pendulum using the 'trapezoidal rule' (Crisfield, 1997), where the solution 'locks' at a position close to the initial position for a certain time step.

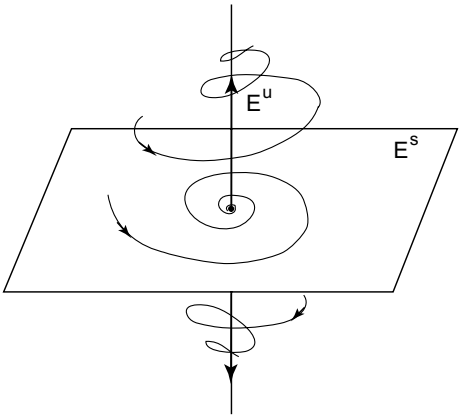

Fig. 1. The stable and unstable subspaces E^{s} and E^{u} for the unstable equilibrium.

This spurious convergence to the unstable solution may be attributable to the coupling effect between the external force and the displacement, and a possible explanation is described as follows.

In the hybrid static–dynamical scheme, a small stepped load increment is applied to the structure so that there may exist an unstable equilibrium which is slightly beyond the secondary bifurcation point and the corresponding stiffness matrix has only one unstable eigenvalue. The local phase portrait for this unstable equilibrium is shown in Fig. 1. For solutions coming close to this point, the tangent stiffness matrix at a given point on the trajectory has an unstable subspace similar to the one shown in Fig. 1. For the mechanical loading case, since the external force is fixed, the displacement increment is solely dependent on the tangent stiffness at the starting point and the initial conditions. Because of the similarity of the unstable subspace, the trajectory can escape exponentially fast from the unstable equilibrium along the unstable subspace. Nevertheless, the situation is different for the thermal case: because of the coupling of the external force with displacement, the displacement increment now depends not only on the tangent stiffness and initial conditions but also on the coupled external force, therefore the solution may be pulled in by the unstable equilibrium and delayed before it finally escapes along the unstable subspace. That is, as time elapses, the trajectory for the coupled system will move slowly along the unstable direction but with all solution components corresponding to the stable subspace converging quickly to the unstable equilibrium solution. This slow escape from the unstable equilibrium point makes the solution seem to converge to the unstable equilibrium point. Numerical examples and more detailed discussion can be found in Section 3.

To overcome this difficulty, we introduce a non-stationary analysis technique which consists of a linear sweep in the load of the form

$$\lambda(t) = \lambda_0 + Rt, \tag{2.1}$$

where λ_0 is the starting load value, R is the load incremental rate and t is the time variable. Under the linear sweep, the undesirable 'locking' phenomenon will not happen. The changing of the load parameter with time not only pushes the trajectory away from the secondary instability point, resulting in more and more unstable eigenvalues appearing in the tangent stiffness matrix along the trajectory, and but also serves as a continuous perturbation source. As a result, the trajectory cannot be *attracted* by a particular unstable point.

2.2. Implicit integration procedure

In this section, it is assumed that all the matrix and vector notations correspond to the global coordinate system. The spatially discrete equations of motion are described in the form

$$\mathbf{M}\ddot{\mathbf{d}} + \mathbf{C}_{\mathrm{d}}\dot{\mathbf{d}} + \mathbf{f}^{\mathrm{i}}(\mathbf{d}) - \mathbf{f}^{\mathrm{e}}(\mathbf{d}, \lambda(t)) = \mathbf{0}, \tag{2.2}$$

where $\mathbf{f}^{\mathrm{i}}(\mathbf{d})$ and $\mathbf{f}^{\mathrm{e}}(\mathbf{d},\lambda(t))$ are the non-linear internal and external load vectors, respectively, and $\mathbf{C}_{\mathrm{d}}$ is the structural damping matrix. For the damping matrix, Rayleigh damping of the following form is assumed:

$$\mathbf{C}_{\mathrm{d}} = c_m\mathbf{M} + c_k\mathbf{K}, \quad \text{with } c_m = 2\pi\zeta_m f_n \quad \text{and} \quad c_k = \zeta_k/2\pi f_n, \tag{2.3}$$

where ζ_m and ζ_k represent the non-dimensional damping ratios for the mass and stiffness matricies, respectively, and f_n represents the fundamental natural frequency at $\lambda = 0$.

The numerical integration scheme consists of a predictor-corrector procedure and is based on the Hilbert–Hughes–Taylor α method (Crisfield, 1997). By introducing the equivalent dynamic residual force $\mathbf{q}(\mathbf{d},\dot{\mathbf{d}},\ddot{\mathbf{d}})$, in the α method, the time-discrete form of (2.2) can rewritten as

$$\mathbf{q}_{n+1} = (1+\alpha)\{\mathbf{f}^{\mathrm{i}}_{n+1} - \mathbf{f}^{\mathrm{e}}_{n+1} + \mathbf{C}_{\mathrm{d}}\dot{\mathbf{d}}_{n+1}\} - \alpha\{\mathbf{f}^{\mathrm{i}}_{n} - \mathbf{f}^{\mathrm{e}}_{n} + \mathbf{C}_{\mathrm{d}}\dot{\mathbf{d}}_{n}\} + \mathbf{M}\ddot{\mathbf{d}}_{n+1} = 0, \tag{2.4}$$

where $-\frac{1}{3} \leqslant \alpha \leqslant 0$ is a free parameter. The above equation is supplemented by Newmarks' time integration scheme:

$$\mathbf{d}_{n+1} = \mathbf{d}_n + \Delta t\dot{\mathbf{d}}_n + \frac{\Delta t^2}{2}\{(1-2\beta)\ddot{\mathbf{d}}_n + 2\beta\ddot{\mathbf{d}}_{n+1}\}, \tag{2.5}$$

$$\dot{\mathbf{d}}_{n+1} = \dot{\mathbf{d}}_n + \Delta t\{(1-\gamma)\ddot{\mathbf{d}}_n + \gamma\ddot{\mathbf{d}}_{n+1}\}, \tag{2.6}$$

where the Newmark constants β and γ are given by

$$\beta = (1-\alpha)^2/4, \quad \gamma = (1-2\alpha)/2. \tag{2.7}$$

In the 'predictor' stage, the tangent stiffness $\mathbf{K}_{T,n}$ is evaluated at the previous time step t_n, i.e., $\mathbf{K}_{T,n} = \dfrac{\partial \mathbf{f}^{\mathrm{i}}}{\partial \mathbf{d}}|_{\mathbf{d}_n}$, and the incremental 'predictor step' $\Delta\mathbf{d}^0_{n+1}$ is solved from the following equation:

$$\overline{\mathbf{K}}_{T,n}\Delta\mathbf{d}^0_{n+1} = \Delta\overline{\mathbf{f}}^{\mathrm{e}}, \tag{2.8}$$

where the equivalent dynamic tangent stiffness matrix $\overline{\mathbf{K}}_{T,n}$ and the equivalent dynamic external force $\Delta\overline{\mathbf{f}}^{\mathrm{e}}$ are defined as

$$\overline{\mathbf{K}}_{T,n} = (1+\alpha)\left(\mathbf{K}_{T,n} + \frac{\gamma}{\beta\Delta t}\mathbf{C}_{\mathrm{d}}\right) + \frac{1}{\beta\Delta t^2}\mathbf{M}, \quad \text{and} \tag{2.9}$$

$$\begin{aligned}\Delta\overline{\mathbf{f}}^{\mathrm{e}} = {} & (1+\alpha)(\mathbf{f}^{\mathrm{e}}_{n+1} - \mathbf{f}^{\mathrm{i}}_{n}) - \alpha(\mathbf{f}^{\mathrm{e}}_{n} - \mathbf{f}^{\mathrm{i}}_{n}) + \mathbf{M}\left(\frac{1}{\beta\Delta t}\dot{\mathbf{d}}_n + \frac{(1-2\beta)}{2\beta}\ddot{\mathbf{d}}_n\right) \\ & + \left[(1+\alpha)\frac{\gamma}{\beta} - 1\right]\mathbf{C}_{\mathrm{d}}\dot{\mathbf{d}}_n + \frac{(1+\alpha)(\gamma-2\beta)}{2\beta}\Delta t\mathbf{C}_{\mathrm{d}}\ddot{\mathbf{d}}_n.\end{aligned} \tag{2.10}$$

To this end, the displacement at the current time step t_{n+1} is updated by $\mathbf{d}^0_{n+1} = \mathbf{d}_n + \Delta\mathbf{d}^0_{n+1}$, while the velocity $\dot{\mathbf{d}}^0_{n+1}$ and the acceleration $\ddot{\mathbf{d}}^0_{n+1}$ are updated according to (2.6) and (2.5), respectively.

In the 'corrector' stage, Newton–Raphson iteration is applied to make the equivalent dynamic residual force $\mathbf{q}_{n+1}$ equal to zero. By applying a truncated Taylor expansion to (2.4), we have the incremental 'corrector' equation as

$$\mathbf{q}^{k+1}_{n+1} = \mathbf{q}^{k}_{n+1} + \left.\frac{\partial\mathbf{q}}{\partial\mathbf{d}}\right|_{\mathbf{d}^k_{n+1}}\delta\mathbf{d}^{k+1}_{n+1} = \mathbf{q}^{k}_{n+1} + \overline{\mathbf{K}}^{k}_{T,n+1}\delta\mathbf{d}^{k+1}_{n+1} = 0, \tag{2.11}$$

where $\delta\mathbf{d}^{k+1}_{n+1}$ is the incremental iterative 'corrector step' at step $n+1$ and iteration $k+1$, while the dynamic tangent stiffness matrix $\overline{\mathbf{K}}^{k}_{T,n+1}$ is now given by

$$\overline{\mathbf{K}}^{k}_{T,n+1} = (1+\alpha)\left(\mathbf{K}^{k}_{T,n+1} + \frac{\gamma}{\beta\Delta t}\mathbf{C}_{\mathrm{d}}\right) + \frac{1}{\beta\Delta t^2}\mathbf{M}. \tag{2.12}$$

The updated quantities can be obtained through the corrector equations resulting from the variational forms of (2.5) and (2.6):

$$\begin{aligned}
\mathbf{d}_{n+1}^{k+1} &= \mathbf{d}_{n+1}^{k} + \delta\mathbf{d}_{n+1}^{k+1},\\
\dot{\mathbf{d}}_{n+1}^{k+1} &= \dot{\mathbf{d}}_{n+1}^{k} + \frac{\gamma}{\beta\Delta t}\delta\mathbf{d}_{n+1}^{k+1},\\
\ddot{\mathbf{d}}_{n+1}^{k+1} &= \ddot{\mathbf{d}}_{n+1}^{k} + \frac{1}{\beta\Delta t^2}\delta\mathbf{d}_{n+1}^{k+1}.
\end{aligned} \tag{2.13}$$

For the convergence test, the norms of the dynamical equivalent residual force and the displacement vectors are checked by the following criteria:

$$\|\mathbf{q}_{n+1}^{k+1}\| \leqslant \epsilon_{\mathbf{f}}\|\mathbf{f}_{n+1}^{\mathrm{e}}\|, \quad \text{and} \quad \|\delta\mathbf{d}_{n+1}^{k+1}\| \leqslant \epsilon_{\mathbf{u}}\|\mathbf{d}_{n+1}^{\mathrm{e}}\|. \tag{2.14}$$

2.3. Automatic time steeping

The linear sweep technique in (2.1) is often combined with a full dynamic integration scheme to analyze the loss of stability of the fundamental path (Virgin and Plaut, 2002). Since mode jumping is often characterized by a transient snap between two 'isolated' stable equilibrium paths of the structure, a very small time step is needed to capture this phenomenon. A commonly used formula to estimate the time step for standard dynamic problems is

$$\Delta t_{\mathrm{dyn}} = 1/(20f), \tag{2.15}$$

where f is the natural frequency of the highest mode that contributes to the response. For the plate models used in this paper, our numerical experiments show that Δt_{dyn} needs be as small as the order of 1.0×10^{-5}–1.0×10^{-4} s in order to satisfy the convergence requirement. Conventional dynamic automatic time stepping schemes such as the one based on the 'current frequency' (Crisfield, 1997) will not improve the computational efficiency for the mode jumping problem, since basically this is still a full dynamic approach and the estimated time step is still very small (on the order of 1.0×10^{-5} s).

Since we are primarily interested in stable equilibrium paths and stability transitions, we require a numerical algorithm that can follow branches accurately and efficiently, including any transient motion initiated due to a local loss of stability. A quasi-dynamic time stepping technique is developed for this purpose.

Let N_k denote the number of iterations needed to approximate the previous continuation step and N_{opt} denote the optimal number of iterations. Then a simple strategy is to reduce the step size in the case $N_k > N_{\mathrm{opt}}$ and increase it when $N_k < N_{\mathrm{opt}}$. This is done with the following formula:

$$\Delta t_{k+1} = \begin{cases} 1/3\Delta t_k & \text{if } \phi < 1/3,\\ \phi\Delta t_k & \text{if } 1/3 \leqslant \phi \leqslant 3,\\ 3\Delta t_k & \text{if } \phi > 3, \end{cases} \tag{2.16}$$

where $\phi = N_{\mathrm{opt}}/N_k$ and Δt_{k+1} denotes the current time step. To distinguish the step size control between the stable path-following phase and that of the transient response, the above standard step control scheme is supplemented by a control on the maximum step size $\Delta t_{\max}$. That is,

$$\Delta t_{\max} = \begin{cases} \Delta t_{\mathrm{mst}} & \text{if } \mathbf{K}_{T,n}^{k} \text{ is positive definite},\\ \Delta t_{\mathrm{mtr}} & \text{if } \mathbf{K}_{T,n}^{k} \text{ is not positive definite}, \end{cases} \tag{2.17}$$

where Δt_{mst} and Δt_{mtr} are the maximum step size assigned to follow the stable equilibrium branches and to ensure the occurrence of the transient response, respectively. The checking of the positive definiteness of the stiffness matrix can easily be achieved by applying Choleski's factorization or a $\mathbf{L}^T\mathbf{D}\mathbf{L}$ factorization. This will not incur additional computational cost since the factorized matrices are also used to obtain the incremental displacement $\Delta\mathbf{d}$ or $\delta\mathbf{d}$. The reason why we enforce the switching of the step size on (2.17) instead of on (2.16) is that we still want to use the standard load step control scheme in the transient response stage to accelerate the convergence of the trajectory to the remote stable branch once the trajectory comes close to it.

To avoid the step size being too big, the traditional bisection technique is adopted, i.e., if a step fails to converge within some maximum number of iterations $N_{\max}$, it will be retried with half the step size. By considering that during the quasi-dynamic sweeping most time is spent on the transient stage, both N_{opt} and $N_{\max}$ are set to be 2. This is because 2 is the minimum iteration number which not only can minimize the computational cost if a step has to be repeated but also has the capability to increase step size automatically.

With (2.17), Δt_{mst} and Δt_{mtr} can be controlled separately. Usually, they are problem dependent and are based on trial and error. However, here we provide some general considerations on how to determine their values. Δt_{mst} and Δt_{mtr} can be determined by the following equations:

$$\Delta t_{\mathrm{mst}} R = \psi_1 \Delta\lambda_{\mathrm{s}}, \quad \psi_1 \leqslant 1, \tag{2.18}$$

$$\Delta t_{\mathrm{mst}} \gg \Delta t_{\mathrm{dyn}}, \tag{2.19}$$

$$\Delta t_{\mathrm{mtr}} = \psi_2 \Delta t_{\mathrm{mst}} \quad \psi_2 \leqslant 1, \tag{2.20}$$

where $\Delta\lambda_{\mathrm{s}}$ is the estimated load step for static analysis which can be obtained by performing the static analysis, generally, a necessary a priori procedure in mode jumping analysis.

Eq. (2.18) means that the dynamic load incremental step for stable-path-following should be slightly less than its static counterpart. A typical value for ψ_1 is 0.05–0.2. The smaller the ψ_1 the more data points can be obtained and the less the possible repeat iterations. Condition (2.19) in conjunction with (2.17) enables the adoption of large time steps to suppress the dynamic response along the stable branches. Moreover, condition (2.19) provides an implicit constraint on the upper bound of R. This is generally preferred in mode jumping analysis, because a large R may cause a large overshoot around the secondary bifurcation point. There is not a strict rule to determine the load incremental rate R. In fact, this algorithm is not sensitive to R, therefore a quite wide range of values can be chosen. In practice, a reasonable value of R can usually be determined by experimental conditions. When the bifurcation point is encountered during the sweep, transient analysis is enforced by the combination of (2.17) with condition (2.20). A typical value for ψ_2 is 0.01–0.1. Although a more strict step control such as $\Delta t_{\mathrm{mtr}} \approx \Delta t_{\mathrm{dyn}}$ can be used in (2.20), taking a large step size even in the transient response phase can increase the dissipation of the kinetic energy for each time step.

3. Results and discussion

3.1. Model description

The methods outlined are used to analyze the mode jumping phenomenon of isotropic aluminum rectangular plates subjected to mechanical and thermal loads. Three plate models and their corresponding boundary conditions are depicted in Fig. 2. In case MeCS, Fig. 2(b), the plate is subjected to the uniformly distributed compressive load $\lambda\widehat{P}$ with λ the load parameter, while in cases ThermSS and ThermCC, Fig. 2(c) and (d), uniformly distributed temperature increase ΔT is applied. Geometries and material properties for these three models are listed in Table 1. It worth noting that for comparison purposes discussed in Part I of this study (Chen and Virgin, in press), different geometries and material properties are selected for the mechanical and the thermal cases. Specifically, MeCS shares the same geometric dimensions and material

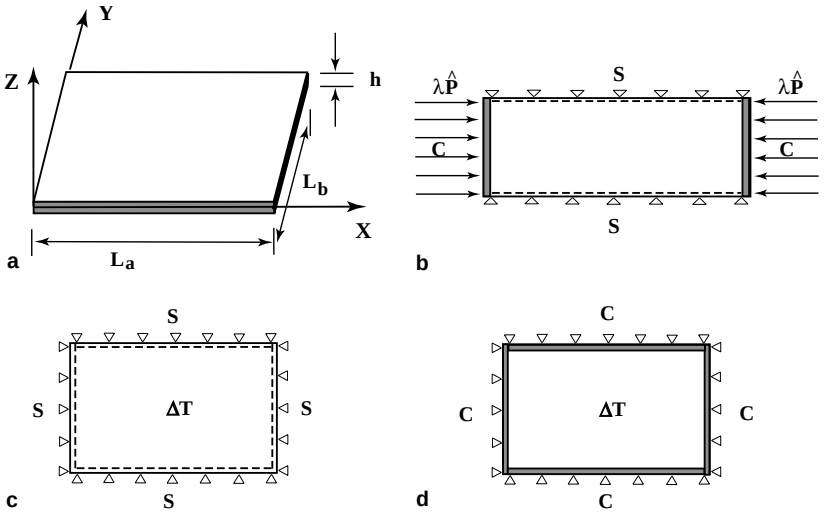

Fig. 2. Plate models and boundary conditions: (a) schematic diagram; (b) case MeCS, shorter edges clamped, longer edges simply supported and in-plane fixed; (c) case ThermSS, four edges simply supported and in-plane fixed; (d) case ThermCC, four edges clamped and in-plane fixed.

Table 1
Geometric dimensions and material properties

Parameter	Mechanical loading MeCS	Thermal loading ThermSS and ThermCC
Length L_a (mm)	644.14	762.00
Width L_b (mm)	119.63	282.22
Thickness h (mm)	1.829	1.984
Aspect ratio $r = L_a/L_b$	5.38	2.70
Young's modulus E (GPa)	70	70
Poison's ratio v	0.3	0.33
Therm-expansion coefficient α ($°C^{-1}$)	23×10^{-6}	23×10^{-6}
Mass density ρ (kg/m^3)	2.790×10^3	2.714×10^3
Damping ratio for $\mathbf{M}$, ζ_m	0.1	0.1
Damping ratio for $\mathbf{K}$, ζ_k	0.2	0.2
Imperfection amplitude[a] A_0 (mm)	10% h	30% h

[a] For case MeCS, the initial imperfection has the form $\mathbf{W}_0 = A_0(\mathbf{v}_{1b} + \mathbf{v}_{2b})$, while for cases ThermSS and ThermCC the form of $\mathbf{W}_0 = A_0\mathbf{v}_{1b}$ is used, where $\mathbf{v}_{1b}$ and $\mathbf{v}_{2b}$ denote the first and the second linear buckling modes of the corresponding *perfect* plate, respectively. $\mathbf{v}_{1b}$ and $\mathbf{v}_{2b}$ are normalized such that $\|\mathbf{v}_{ib}\|_\infty = 1$, $i = 1, 2$, where $\|\mathbf{v}_{ib}\|_\infty = \max\{\mathbf{v}_{ib} \cdot \mathbf{e}_k\}$, $k = 1, 2, \ldots$.

properties as Stein's experimental model, while the plate used in ThermSS and ThermCC is identical with the one in the reference Chen and Virgin (2004).

For Rayleigh damping defined in Eq. (2.3), damping coefficients c_m and c_k are selected by analogy to a linear, single degree-of-freedom oscillator, leading to the equivalent non-dimensional damping ratio $2\xi = \xi_m + \xi_k$ (Muheim and Johnson, 2003). Specifying $\xi_m = 0.1$ and $\xi_k = 0.2$ in Table 1 leads to $\xi = 0.15$, which is within the recommended range of $0.05 < \xi < 0.20$ from the reference Riks et al. (1996) (in which $\xi = \xi_m = \xi_k = 0.1$ is assumed).

HC finite element descretization is used to obtain numerical solutions and mesh sizes for three plate models are determined by convergence tests. As results in Part I shows that mesh sizes 49×9 and 40×12 are sufficient for the mechanical loading and thermal loading cases, respectively, the following analysis is carried out using these mesh sizes. For more discussions on the plate model, one may consult Part I.

3.2. Summary of local post-secondary bifurcation analysis

This subsection provides a brief overview of the local post-secondary analysis results obtained by using asymptotic finite element analysis developed in Part I. The first and secondary buckling loads as well as the secondary bifurcation type for each of three plate models are shown in Table 2.

It is observed from Table 2 that the secondary bifurcation of the uniaxially compressed plate, MeCS, occurs at a load level about 1.75 times that of the primary buckling load ($N_{b1}/N_{b2} = 1.75$). Whereas, for the four-edge in-plane fixed thermally loaded plates, the secondary bifurcation point of occurs much further beyond its primary buckling point, with $\Delta T_{b2}/\Delta T_{b1}$ being 9.90 in ThermCC and 44.15 in ThermSS. This may be attributed to the strong geometric non-linearity caused by the boundary constraints (both in-plane and out-of-plane) (Chen and Virgin, 2004). Because of the intensive coupling between the external load and the displacement field, the thermally buckled plate demonstrates much stronger geometric non-linearity than the mechanically loaded case. Therefore, the analysis of the mode jumping of the former cannot be handled easily by using the equivalent bi-axially compressed mechanical model with simple linear relations between the longitudinal and transverse edge forces.

Initial post-secondary bifurcation behaviors are studied by using the perturbation method introduced in Part I. Bifurcation types listed in Table 2 are determined by calculating the bifurcation coefficients using a single mode analysis approach. Three typical bifurcation types—asymmetric, subcritical and supercritical, are found for plates with different combinations of load types and boundary conditions. The initial post-secondary bifurcated paths and their stability are analyzed by using a multi-mode dynamic reduction method. Results show that for the asymmetric bifurcation case, MeCS, the stable bifurcated path quickly loses its stability beyond the secondary bifurcation point, with $N_x - N_{b2} \approx 0.0175$ N/mm or $\Delta N_x/N_{b1} \approx 2.45 \times 10^{-4}$. Therefore, strictly speaking the mode jumping occurs slightly beyond the secondary bifurcation point.

Bifurcation diagrams (not show here) obtained by the multi-mode dynamic reduction method reveal that the thermally loaded plates experience subcritical and supercritical post-secondary bifurcation behaviors, thus confirming the single model analysis result. The post-secondary bifurcation and mode jumping is revealed by the load vs. displacement relations in Fig. 3. For comparison purposes, results for ThermSS are obtained by the analytic method developed in our previous paper (Chen and Virgin, 2004) to overcome the limitations of the local perturbation approach. With regards to the asymptotic bifurcation case, MeCS, because the stable post-secondary buckling branch loses its stability immediately after the secondary point ($\Delta N_x/N_{b1} = 2.45 \times 10^{-4}$) and the local perturbation analysis cannot capture the remote stable branch to which the plate may jump, no corresponding load vs. displacement plot is provided.

Fig. 3(a) exhibits a complicated post-secondary bifurcation behavior for the thermally loaded simply supported plate. Near the secondary buckling load $\Delta T_{b2} = 69.31$ °C, the bifurcation is subcritical but the unstable bifurcated paths are blocked by further bifurcation points; as a result, three unstable bifurcation paths are needed to connect the fundamental path and the remote stable target branch, demonstrating the existence of strong non-linearity. In Fig. 3(b) the multi-mode perturbation analysis provides qualitatively

Table 2
The primary and second buckling loads of three plate models

Cases	First buckling load[a] $N_{b1}(\Delta T_{b1})$	Secondary buckling load[b] $N_{b2}(\Delta T_{b2})$	Load ratio N_{b2}/N_{b1} $(\Delta T_{b2}/\Delta T_{b1})$	Secondary bifurcation types
MeCS	77.937 N/mm	136.19 N/mm	1.747	Asymmetric
ThermSS	1.518 °C	67.04 °C	44.15	Subcritical
ThermCC	5.279 °C	52.29 °C	9.90	Supercritical

[a] The first buckling load is obtained from the corresponding perfect plate.
[b] The second buckling load is the *primary* buckling load obtained in the fully geometrically non-linear analysis of the *imperfect* plate.

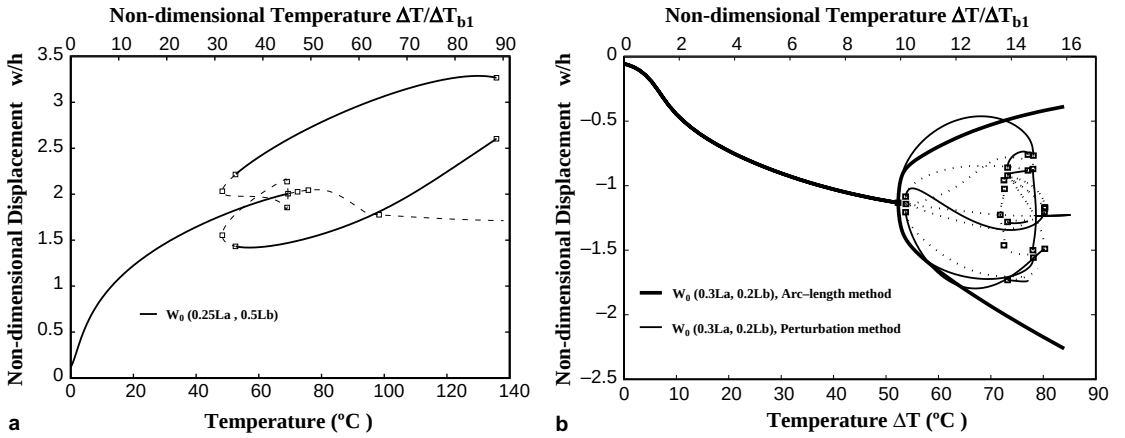

Fig. 3. Subcritical and Supercritical post-secondary bifurcations for plates under thermal loading: (a) case ThermSS, analytical method using 27 global linear buckling modes (Chen and Virgin, 2004), (b) case ThermCC, perturbation method with multi-mode dynamic reduction, 6 modes. Stable paths are shown as solid lines and unstable paths as broken lines.

the post-secondary buckling behavior of the four-edge clamped plate, ThermCC. At $\Delta T_{b2} = 52.29$ °C or $\Delta T_{b2}/\Delta T_{b1} = 9.90$, two stable branches bifurcate from the secondary bifurcation point. Slightly above the bifurcated point, at $\Delta T = 53$ °C, another pair of branches emanate from the fundamental path and are initially unstable. More stable branches appear as the temperature reaches 72 °C. Mode-jumping is observed at $\Delta T = 78$ °C, where the first pair of stable branches lose their stability and the plate will 'jump' to a remote state on one of the still stable branches. Note that the perturbation method has been used as a branch-switching technique to obtain arc-length results shown in Fig. 3(b). When compared to arc-length, the perturbation results show good agreement up to 8 °C above the secondary bifurcation point.

A close scrutiny of Fig. 3 also reveals an interesting phenomenon: for the thermally loaded plate, after the passing of the secondary bifurcation point, stable equilibrium paths appear in pairs and each pair seems to demonstrate some kind of symmetry with respect to the fundamental path. As we will show later, this kind of symmetry actually reflects the fact that moving along a pair of stable paths (supercritical pair for ThermCC or the remote target one for ThermSS), the frequencies of the plate at the two corresponding points on that pair are identical.

3.3. Spurious convergence

In the hybrid static–dynamic method, the static analysis approach is stopped when the secondary bifurcation point is encountered. Then a small stepped load increment is applied and a dynamic analysis approach is adopted to simulate the 'jumping' of the equilibrium position to a remote stable branch. In this paper, this is accomplished by using the Hilbert–Hughes–Taylor α method. For both the mechanically loaded plate, MeCS, and the thermally one, ThermSS, various different choices of parameters such as the load step $\Delta\lambda$ or ΔT, the size of the time step (with and without the automatic time stepping), the coefficient α, and the kinetic energy threshold have been tried. It is interesting to note that by using the above integration scheme, the remote stable state can always be found for MeCS while for ThermSS the solution often seems to converge to an unstable equilibrium position on the fundamental path. In Section 2.1, the spurious convergence phenomenon was explained by the slow movement of the trajectory along the unstable subspace of the unstable equilibrium due to the coupling effect between the external force and the displacement. To verify this claim, a typical numerical example for the thermally loaded plate (ThermSS) is presented in

Fig. 4, with parameters as shown. As regards the automatic time stepping, a technique based on the 'current frequency' (Crisfield, 1997),

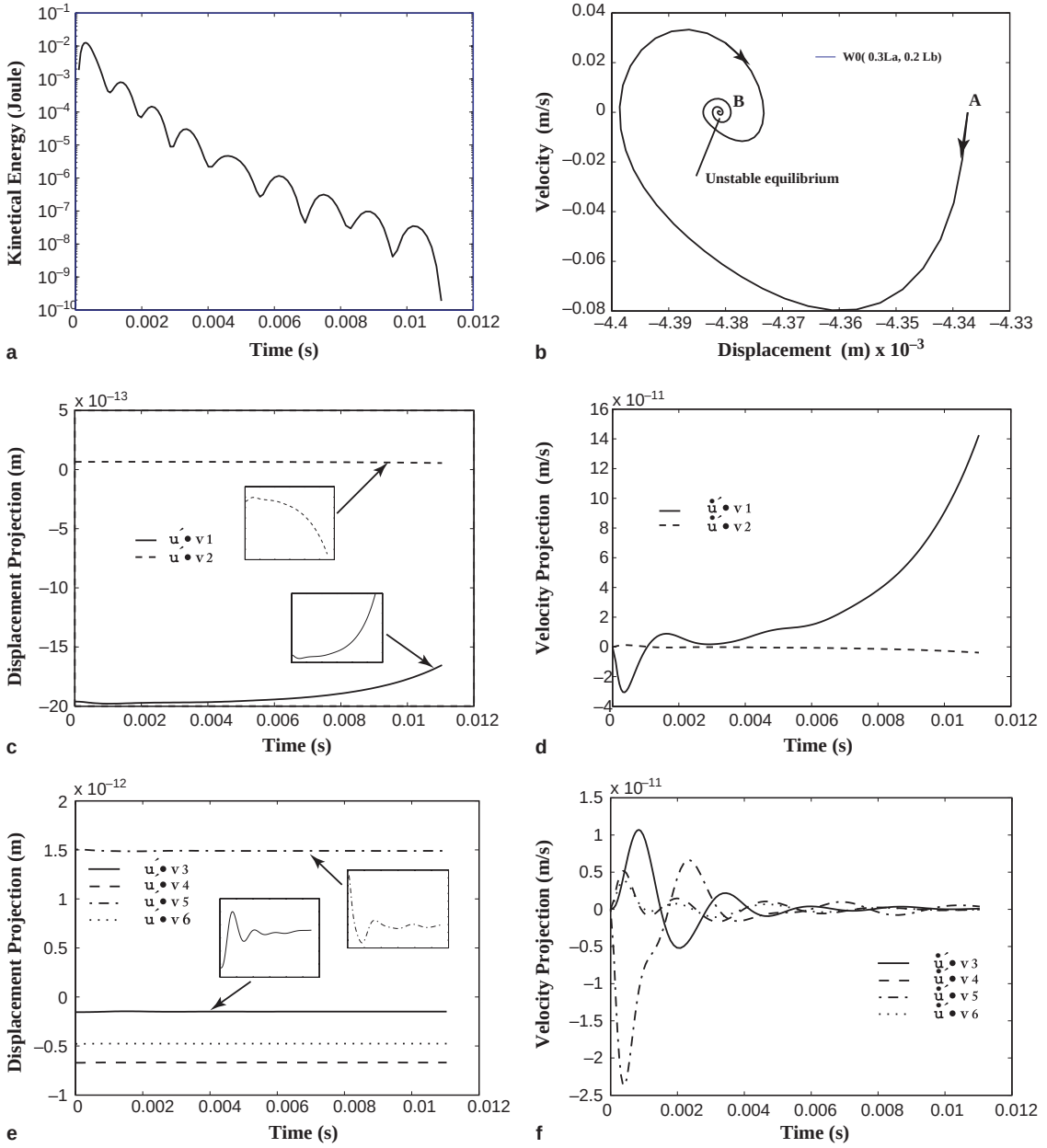

Fig. 4. Spurious Convergence of the transient response to an unstable equilibrium point using hybrid static–dynamic approach, case ThermSS, load step = 1.5 °C, $\alpha = -0.05$, automatic time stepping, energy threshold $K_{\text{thres}} = 1.0 \times 10^{-10}$ J. (a) Kinetic energy; (b) phase portrait; (c) projection of the displacement $\mathbf{u}$ onto the unstable subspace $E^{\text{u}} = \{\mathbf{v}_1, \mathbf{v}_2\}$; (d) projection of the velocity $\dot{\mathbf{u}}$ onto the unstable subspace $E^{\text{u}} = \{\mathbf{v}_1, \mathbf{v}_2\}$; (e) projection of the displacement $\mathbf{u}$ onto the stable subspace $E^{\text{s}} = \{\mathbf{v}_3, \mathbf{v}_4, \mathbf{v}_5, \mathbf{v}_6\}$; (f) projection of the velocity $\dot{\mathbf{u}}$ onto the stable subspace $E^{\text{s}} = \{\mathbf{v}_3, \mathbf{v}_4, \mathbf{v}_5, \mathbf{v}_6\}$.

$$\omega^2 = \frac{\Delta\mathbf{d}^{\mathrm{T}}\mathbf{K}\Delta\mathbf{d}}{\Delta\mathbf{d}^{\mathrm{T}}\mathbf{M}\Delta\mathbf{d}}, \quad \Delta t_{\mathrm{new}} = 0.05\frac{2\pi}{|\omega^2|},$$

is used.

Fig. 4(a) and (b) give a sense of the spurious convergence. Starting from the current equilibrium position A, the trajectory seems finally to converge to a remote point B, as if it is a regular stable equilibrium. In the meantime, the kinetic energy first evolves to the maximum value, then keeps oscillating and decaying until the threshold is met, with $K_{\mathrm{end}}/K_{\max} = 1.50 \times 10^{-8}$. However, a close examination of the tangent stiffness matrix at point B shows that there exist two negative eigenvalues, indicating that point B is actually an unstable equilibrium. To study this spurious attraction, we project the displacement and velocity vectors $\mathbf{d}$ and $\dot{\mathbf{d}}$ onto the unstable and the stable subspaces E^{u} and E^{s}, respectively. For simplicity, only the first six eigenpairs—$(r_1, \mathbf{v}_1)$, $(r_2, \mathbf{v}_2), \ldots, (r_6, \mathbf{v}_6)$, are used, with $r_1 = -648.9$, $r_2 = -423.7$, $r_3 = 3574.9$, $r_4 = 8171.4$, $r_5 = 8237.0$ and $r_6 = 9102.2$, respectively. Thus, $E^{\mathrm{u}} = \{\mathbf{v}_1, \mathbf{v}_2\}$ and $E^{\mathrm{s}} = \{\mathbf{v}_3, \mathbf{v}_4, \mathbf{v}_5, \mathbf{v}_6\}$. A close examination of Fig. 4(c) and (e) reveals that as time elapses the displacement projections on the unstable eigenvectors keep increasing or decreasing while the projections onto the stable subspace oscillate, decay and finally converge. An even clearer picture is reflected by the velocity projections in Fig. 4(d) and (f). Although the velocity projections on the stable subspace eventually decay to zero, those on the unstable subspace remain consistently rising or falling, even if the kinetic energy becomes very small. It is this slow escape of the trajectory from the unstable subspace of the point B that causes the spurious convergence.

3.4. Non-stationary sweep

The non-stationary sweep method outlined before is used to analyze mode jumping for the three plate models. Starting from an equilibrium position on the fundamental path, the plate is subjected to a linear load sweep with a constant incremental rate R. At first, the load is increased to pass the secondary bifurcation point so that the plate will 'jump' dynamically to a remote stable branch. Then, we decrease the load with the same R and expect the plate to 'jump' back to its fundamental path.

For the case ThermSS, in the ascending stage the temperature rises from 60 °C (90% ΔT_{b2}) to 80 °C (110% ΔT_{b2}), with $R = 10$ °C/s, while during the descending procedure the temperature drops from 80 °C to 27 °C (40% ΔT_{b2}), with the same R. The maximum allowable time steps to encourage the stable-path-following and to enforce the transient switching in the quasi-dynamic analysis are set at $\Delta t_{\mathrm{mst}} = 0.02$ s and $\Delta t_{\mathrm{mtr}} = 0.002$ s, respectively. Although for the given incremental ratio, larger step sizes such as $\Delta t_{\mathrm{mst}} = 0.2$ s and $\Delta t_{\mathrm{mtr}} = 0.02$ s also work, the main purpose of our choosing the smaller values is to provide enough data points (temporal resolution) for the later natural frequency analysis.

Fig. 5 provides a 3-D phase plot and the time history of kinetic energy during the ascending stage while the hysteretic behavior of the plate is depicted in Fig. 6. Stable equilibrium branches, both before and after the mode jumping, are captured with good accuracy, demonstrated by the small values of kinetic energy in the path-following procedures and the overlapping of the static and quasi-dynamic results when the displacement jumps back to its fundamental path. From Fig. 5(a), it is observed that the trajectory at first follows the stable static equilibrium branch until the occurrence of the secondary instability point, $\Delta T_{\mathrm{b2}} = 67.04$ °C. Then it escapes from the unstable fundamental path, spins around a remote stable equilibrium branch for a while, jumps to another stable one and finally follows the latter. The stability of the two stable equilibrium branches are confirmed by monitoring the positive-definiteness of the stiffness matrices during the snap, which is indicated by the solid circles in Fig. 6(a). It is interesting to note that the dynamic jump in fact involves the interaction between a pair of remote stable target branches, see Fig. 3(a). The two pulses appearing in the energy plot, Fig. 5(b), reflect the escaping nature of the trajectory from the unstable fundamental path and from one of the stable target branches. During the descending stage, the target branch loses its stability at $\Delta T = 51$ °C, then, after an intermediate jump, the plate jumps back to

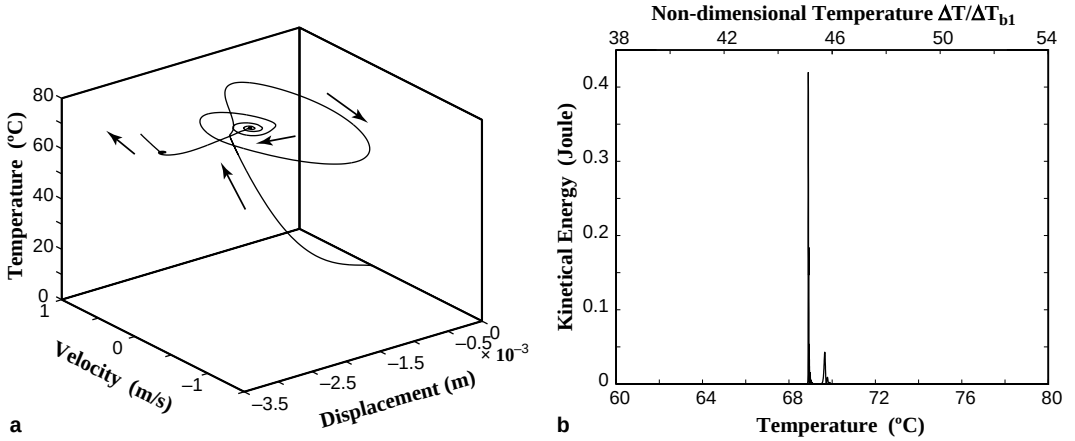

Fig. 5. Phase and kinetic energy plots during the ascending stage, case ThermSS. (a) 3-D phase plot; (b) kinetic energy during sweeping.

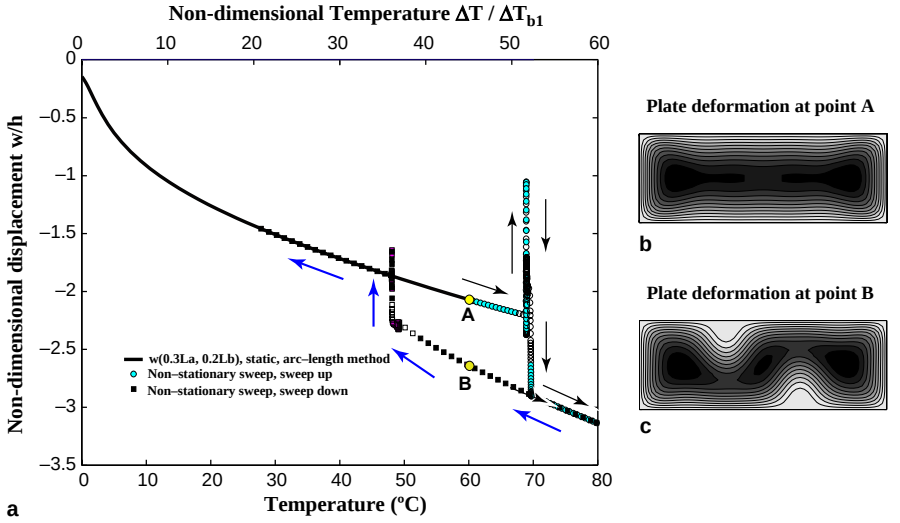

Fig. 6. Quasi-dynamic response of a thermally loaded plate with four edges simply supported, case ThermSS, non-stationary sweep method, $R = \pm 10$ °C/s, $\Delta t_{\mathrm{mst}} = 0.02$ s, $\Delta t_{\mathrm{mtr}} = 0.002$ s. (a) Vertical displacement at $w(0.3L_a, 0.2L_b)$; (b) plate deformation at point A; (c) plate deformation at point B. Solid symbol represent stable state; hollow symbols represent unstable state.

its fundamental path at 48 °C, see Fig. 6(a). The development of the bucking patterns are also checked carefully. Along the fundamental path, the pattern evolves smoothly from the (1,1) mode (due to the initial imperfection) to the complicated 'symmetric bottles' indicated by Fig. 6(b), with their displacement contours symmetric with respect to both the x- and y-axes. However, after the mode jumping, this kind of symmetry is broken and the buckling pattern changes dramatically to the 'oblique bumps', with the displacement contours now symmetric with respect to the center of the plate, Fig. 6(c).

For the four edges clamped case, ThermCC, the mode jumping occurs at the tertiary bifurcation point, $\Delta T_{b3} \approx 84$ °C, therefore the linear sweep starts at an equilibrium position on one of the stable post-secondary bifurcated branches. During the ascending stage the temperature rises from 75 °C (90% ΔT_{b3}) to 100 °C (120%

ΔT_{b3}), with $R = 10$ °C/s, while during the descending procedure the temperature drops from 100 °C to 45 °C (54% ΔT_{b3}), with the same R. The results are presented in Fig. 7. It can be observed from Fig. 7(a) that although there is a delay or over-shoot between the loss of stability of the stable branches and the dynamic snap during both the ascending and descending procedures, by monitoring the positive-definiteness of the stiffness matrix our algorithm predicts accurately when these instabilities will happen—the stable post-secondary bifurcation path becomes unstable when ΔT reaches 84 °C while the target stable branch becomes unstable when ΔT reduces to 72 °C. This agrees well with the previous multi-mode perturbation analysis which reveals in Fig. 3(b) that multiple stable branches coexist when the temperature is above 72 °C. Interestingly, during the descending procedure, after the mode jumping, the solution follows the post-secondary bifurcated branch, passes the secondary bifurcation point and continues to follow the fundamental branch.

The most intriguing finding is the propagation of the buckling patterns during the temperature sweep. Again, along the fundamental path the buckling pattern of the plate demonstrates symmetry with respect to both the x- and y-axes, Fig. 7(b). The secondary bifurcation point indicates the breaking of symmetry in the y-direction—two buckled patterns on point B and C in Fig. 7(c) and (d) are only symmetric with respect to the y-axis. Interestingly, each of the two buckled patterns seems to come from flipping its counterpart about the center line parallel to the x-axis. The breaking of symmetry continues when the tertiary bifurcation is encountered. The buckled pattern on the remote target path demonstrates the breaking of symmetry in both the x- and y-axes—displacement contours now exhibit the 'worm-like' pattern and again are symmetric with respect to the center of the plate.

The non-stationary sweep results of the uniaxially compressed plate, case MeCS, are provided in Fig. 8. The load sweep starts at $N_x/N_{b1} = 1.5$, at first increases to $N_x/N_{b1} = 2.0$ with $R/N_{b1} = 0.2$ (1/s) then reduces to $N_x/N_{b1} = 1.1$ with the same R. Again the hysteretic behavior is captured by the non-stationary sweep. In contrast with the free-straight-longer-edges case (Stein's experiment), in which the mode jumping demonstrates the transition of bucked patterns of the plate from mode (5, 1) to (6, 1) (Riks et al., 1996), the buckled patterns for MeCS now snap from mode (4, 1) to (5, 1), see Fig. 8(b) and (c). Thus, the secondary bifurcation point for the uniaxially loaded plate often indicates the increment of the wave number by one.

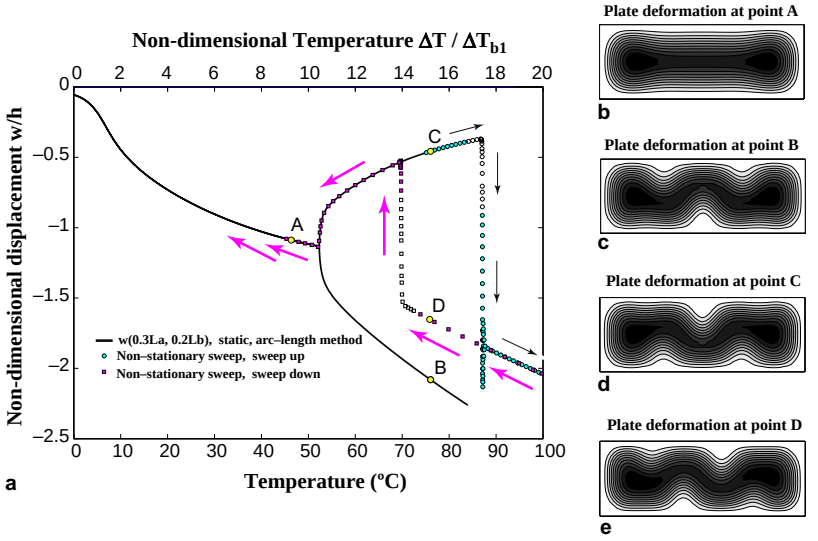

Fig. 7. Quasi-dynamic response of a thermally loaded plate with four edges clamped, case ThermCC, non-stationary sweep method, $R = \pm 10$ °C/s, $\Delta t_{mst} = 0.02$ s, $\Delta t_{mtr} = 0.002$ s. (a) Vertical displacement at $w(0.3L_a, 0.2L_b)$; (b–e) represent the plate deformation at point A–D, respectively. Solid symbol represent stable state; hollow symbols represent unstable state.

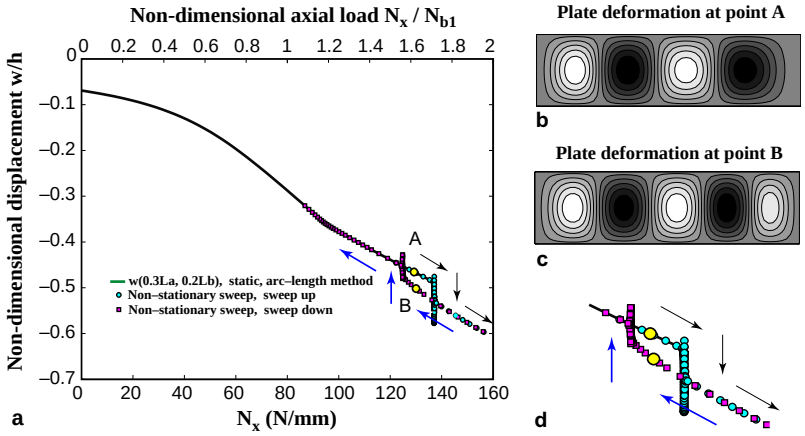

Fig. 8. Quasi-dynamic response of an uniaxially compressed plate, case MeCS, non-stationary sweep method, $R = \pm 1.70 \times 10^4$ N/ms, $\Delta t_{mst} = 0.01$ s, $\Delta t_{mtr} = 0.001$ s. (a) Vertical displacement at $w(0.3L_a, 0.2L_b)$; (b) plate deformation at point A; (c) plate deformation at point B; (d) zoom of the hysteretic behavior; (d) enlargement. Solid symbol represent stable state; hollow symbols represent unstable state.

3.5. Vibration behavior

Natural frequencies and vibration modes are calculated as we trace the equilibrium before and after the mode jumping. Specifically, the lowest three natural frequencies and the corresponding vibration modes on the fundamental equilibrium path and the remote target path are computed based upon the previous non-stationary sweep results. Since we focus only on stable solutions, the computation is performed only when the stiffness matrix is positive definite. For three load cases, the first three natural frequencies on the fundamental path and the jumped path are depicted in Figs. 9–11, where eigenvalue curves are labelled by their order, not by mode.

Free vibration results for the simply supported plate, ThermSS, can be found in Fig. 9. The comparison of the natural frequencies obtained by the non-stationary sweep method, Fig. 9(a), with those by the analytic method, Fig. 9(b), shows good agreement. It is worth mentioning that because the two stable target branches demonstrate some kind of symmetric relationship (see Fig. 3(a)), at the corresponding points on these branches the natural frequencies are identical. The effect of the primary and the secondary bifurcation points on the natural frequencies can be observed clearly in Fig. 9(a). When the temperature increases to its primary buckling value (1.5 °C), natural frequencies drop initially then increase. However, when the secondary buckling temperature (67 °C) is reached the first natural frequency drops to zero and all three natural frequencies jump to their new values on the remote path. During the reverse sweep procedure, three natural frequencies drop consistently until the current branch loses its stability at 52 °C, where the first natural frequency tends to zero, then they jump back to their original values on the fundamental path.

Another interesting phenomenon that can be found is the 'mode shifting', as mentioned in Chen and Virgin (2004). It can be observed in Fig. 9(a) that in the primary post-buckling range there exist several compound points where the first and the second natural frequency curves intersect. Between two neighboring compound points, the fundamental mode shape remains similar, but as they are passed from the left the fundamental mode shape will change to a form corresponding to a previously higher frequency. A quick examination shows that no such 'mode shifting' can be found on the jumped paths. In Fig. 9(a) seven points are assigned to reveal this 'mode shifting' and to disclose the vibration mode shape after

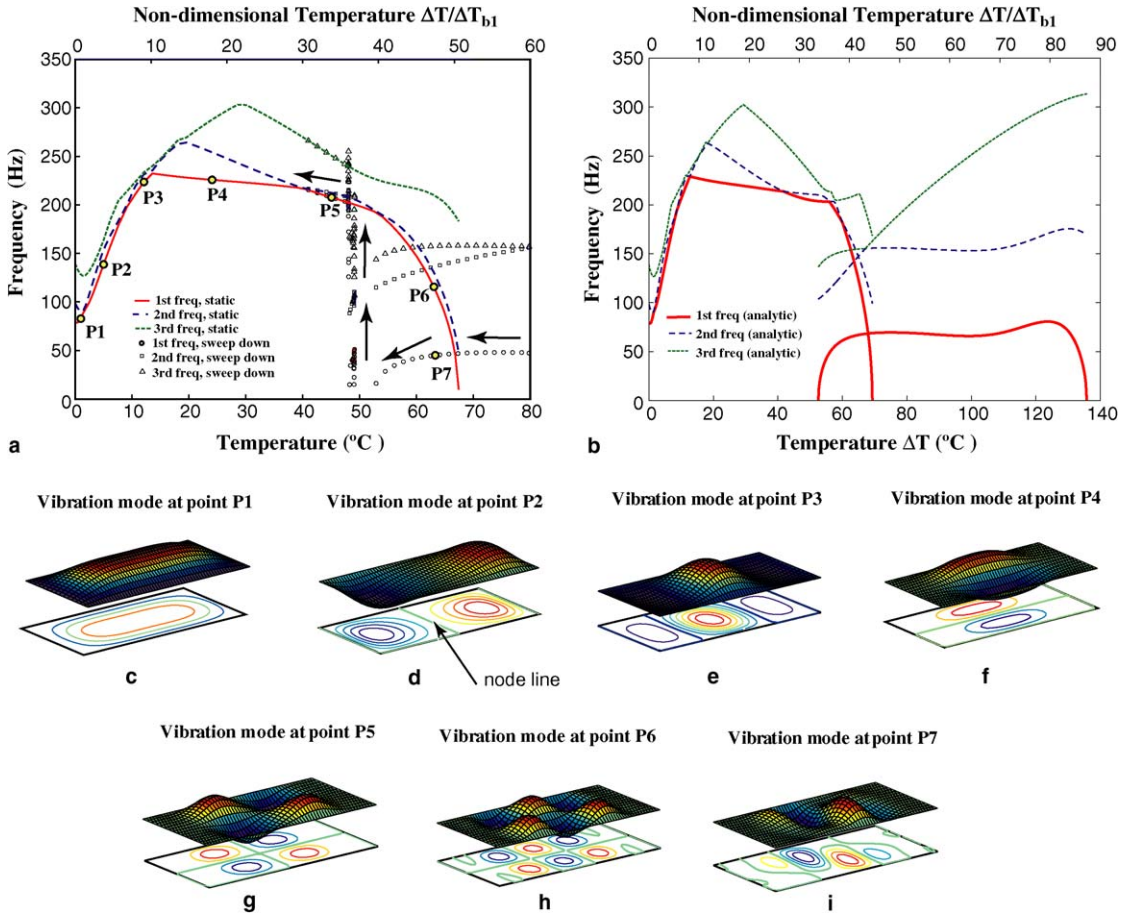

Fig. 9. The first three natural frequencies on the fundamental path and the jumped path with the lowest vibration modes at given points, case ThermSS. (a) Quasi-static and non-stationary sweep finite element methods; (b) analytic method with 27 global modes (Chen and Virgin, 2004); (c–i) lowest vibration modes at points $P1$–$P7$, respectively.

mode jumping. Fig. 9(c)–(h) illustrate the changing of vibration modes from (1, 1) to (2, 1) and higher modes. Like their static deformation forms (or buckling patterns) discussed in the previous section, all the vibration modes obtained about the equilibrium points on the fundamental path demonstrate double symmetry, i.e., their contour plots are symmetric with respect to both the x- and y-axes. In addition, the node lines of the plate remain straight. Similarly, such symmetry is destroyed by the occurrence of the secondary instability and the mode jumping. Instead of exhibiting x and y symmetry, the contour plot of the vibration mode on the target path (see Fig. 9(i)) now demonstrates the symmetry with respect to the center of the plate, with the node lines being distorted and curved.

Natural frequencies and vibration modes for the four-edge-clamped plate, ThermCC, are reported in Fig. 10. The lowest natural frequency drops to zero at 52 °C, 84 °C and 70 °C, corresponding to the secondary and tertiary bifurcation points and the point where the jumped path loses its stability. The lowest frequency reduces in the vicinity of initial buckling but initial imperfections prevent it from going to zero (near 5 °C). Again, the 'mode shifting' phenomenon is observed on the primary post-buckling regime. However, there is no evidence that such shifting occurs on the stable post-secondary bifurcation path or the remote jumped

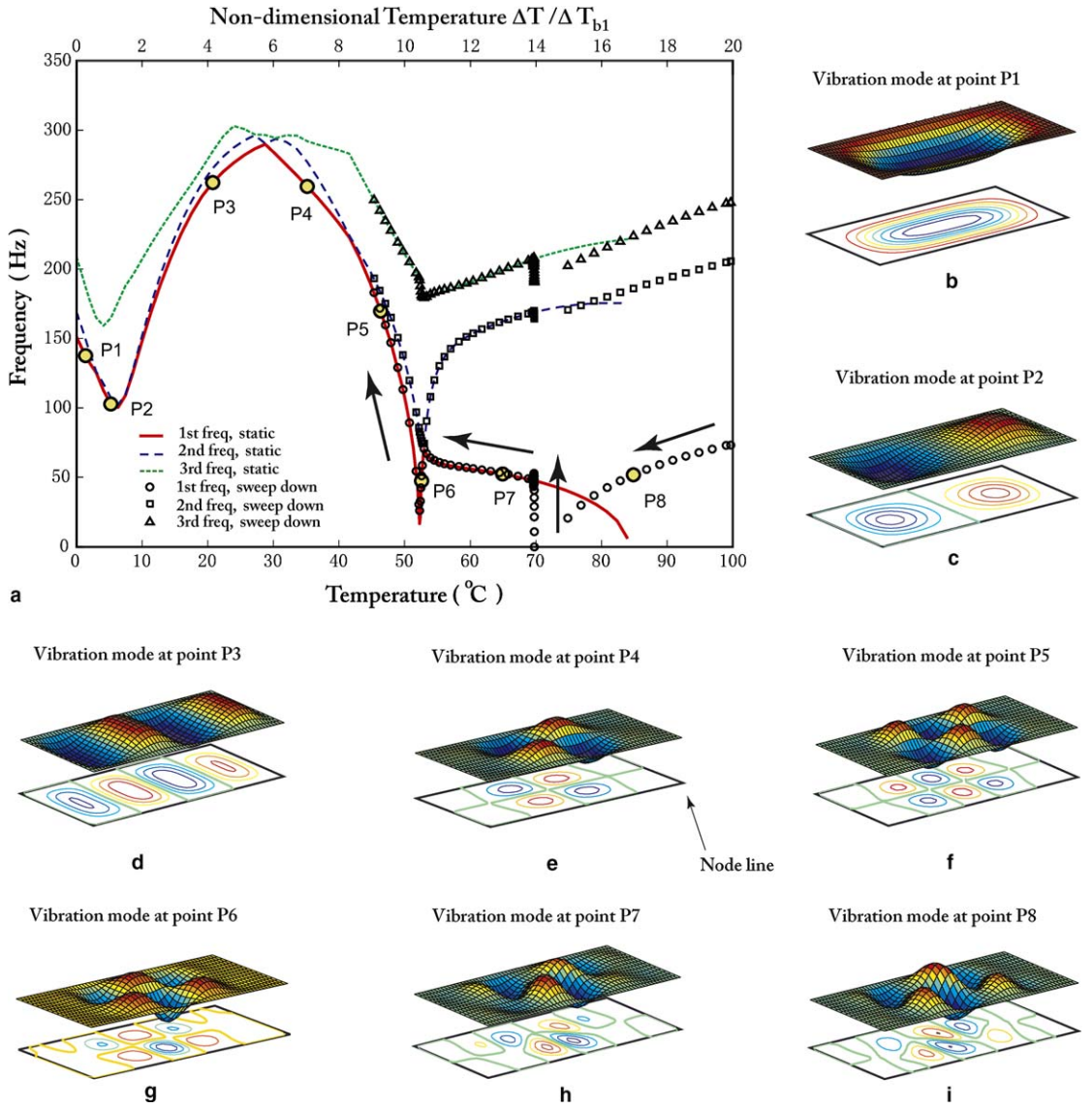

Fig. 10. The first three natural frequencies on the fundamental path and the jumped path with the lowest vibration modes at given points, case ThermCC. (a) Quasi-static and non-stationary sweep finite element methods; (b–i) lowest vibration modes at points $P1$–$P8$, respectively.

path. The investigation of the lowest vibration modes on the fundamental path, Fig. 10(b)–(f), illustrates the 'mode shifting' phenomenon. Moreover, all these modes demonstrate the double symmetry with respect to both the x- and y-axes and the node lines remains straight, just like in the simply supported case, ThermSS. Nevertheless, a different situation happens when the secondary instability is encountered—the secondary bifurcation point now designates the breaking of symmetry only with respect to the x-axis. Contour plots of the vibration modes of the points $P6$ and $P7$ on the post-secondary bifurcation path show symmetry only with respect to the y-axis, see Fig. 10(g) and (h). The tertiary bifurcation point continues this symmetry break-

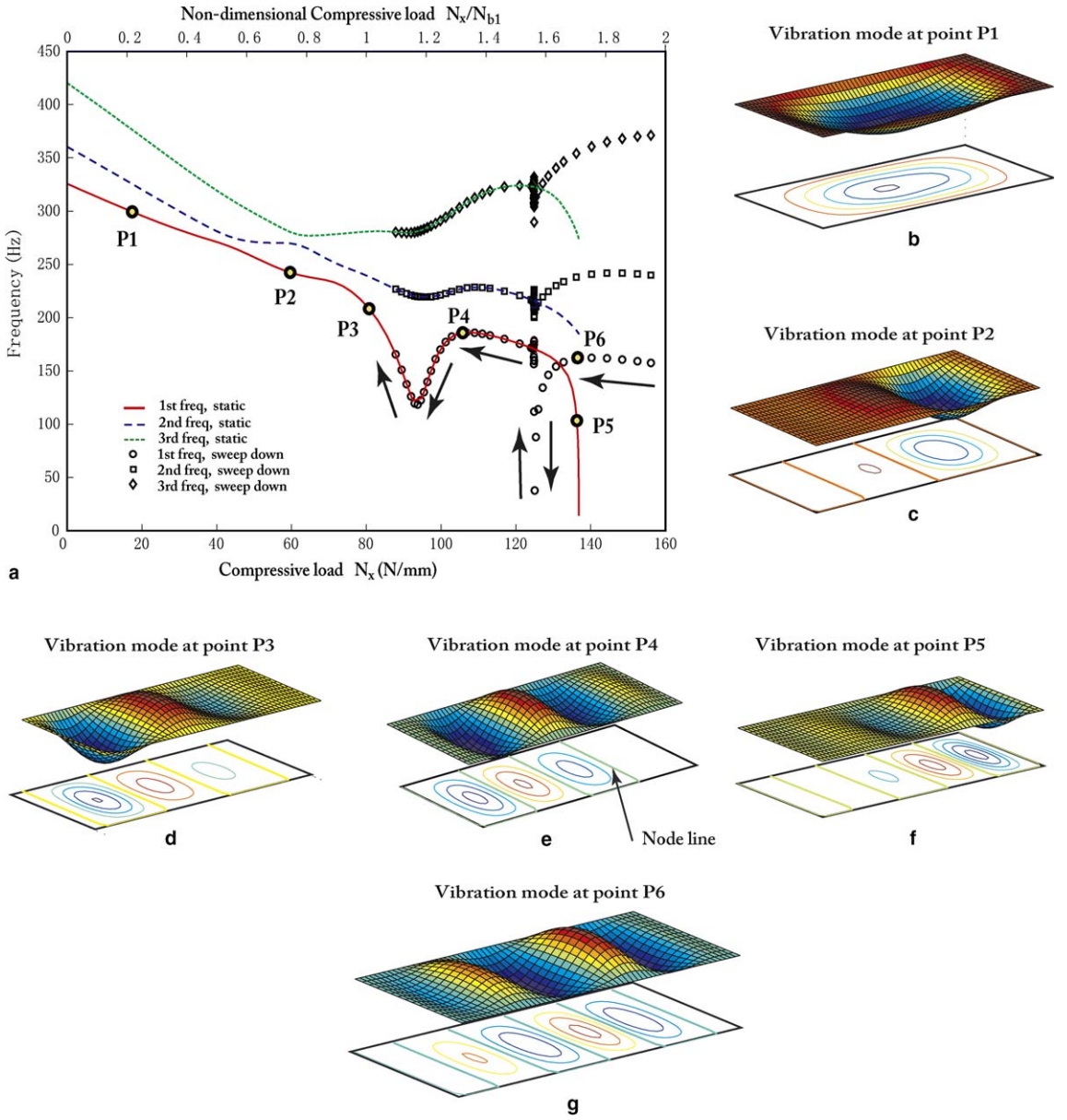

Fig. 11. The first three natural frequencies on the fundamental path and the jumped path with the lowest vibration modes at given points, case MeCS. (a) Quasi-static and non-stationary sweep finite element methods; (b–g) lowest vibration modes at points *P*1–*P*6, respectively.

ing—the *y* symmetry is finally broken by the occurrence of the mode jumping. The contour plot of the lowest vibration mode at point *P*8 on the remote buckled path, Fig. 10(i), now demonstrates symmetry with respect to the center of the plate and again the node lines are distorted and become node curves.

Fig. 11 provides the results for the mechanically loaded plate, MeCS. The lowest natural frequency drops to zero at $N_x/N_{b1} = 1.7$ and $N_x/N_{b1} = 1.6$, respectively, corresponding to the two compressive load levels where mode jumping emerges. Although no obvious 'mode shifting' can be found in the frequency

plot, the tendency of the exchange of the first and second, the second and the third, and again the first and the second vibration modes can be observed roughly at $N_x/N_{b1} = 0.6$, 0.8, and 1.0, respectively, in Fig. 11(a). This kind of curve veering may be caused by the initial imperfection of the plate. A similar phenomenon is also found in an axially compressed braced column (Plaut et al., 1995). On the fundamental path, the lowest vibration modes changes from (1, 1) mode at $P1$, to (3, 1) mode at $P2$ and finally to (5, 1) mode at $P5$, slightly before the bifurcation point. After the mode jumping the vibration mode at $P6$ shows an increment of one wave number, i.e., the (6, 1) mode. The secondary bifurcation points do not reveal any obvious breaking of symmetry in the physical sense.

4. Concluding remarks

A complete investigation of post-buckling behaviors (including post-buckling dynamics and mode jumping) of generally loaded rectangular plates is achieved by combining the local post-secondary analysis with a global non-stationary study. Secondary bifurcation types and the initial post-secondary buckling behaviors are determined by applying an asymptotic finite element analysis approach introduced in Part I, while an adaptive non-stationary load sweeping algorithm is developed to analyze the mode jumping in a global context. With the utilization of an automatic time stepping scheme, the non-stationary procedure has the merits of adapting large load steps to capture the static characteristics of the stable equilibrium paths both before and after mode jumping and reducing automatically the step size to ensure the dynamical transition between the two stable branches. Thus, it is computationally effective.

Three typical instability types—asymmetric, supercritical and subcritical bifurcations are observed according to the different combinations of boundary conditions and load types. Various subsequent buckling patterns, such as 'bumps' for the uniaxially compressed plate, 'oblique bumps' for the thermally-loaded simply supported plate and the 'worm-like' for the thermally-loaded clamped plate occurring after the mode jump are also found. While the mode jumping for the mechanically-loaded plate corresponds to the increase of the wave number of the static deformation along the longitudinal direction, the dynamic snap for the thermally-loaded plates demonstrates the breaking of symmetry of the post-buckled shapes: on the fundamental path the static deformation is symmetric to both the x- and y-axes; after the mode jumping the deflection is found to be antisymmetric to both the x- and y-axes, i.e., it is now symmetric with respect to the center of the plate. Particularly, for the thermally-loaded four-edge clamped plate, such breaking of symmetry consists of two continuous morphological mutations of the post-buckled patterns—the secondary bifurcation point indicates the breaking of the symmetry with respect to only the x-axis while the tertiary bifurcation point designates the destruction of symmetry with respect to both the x- and y-axes.

Spurious convergence phenomenon found in the transient analysis procedure in the hybrid static–dynamic method is explained by the slow movement of the trajectory along the unstable subspace of an unstable equilibrium due to the coupling effect between the external force and the displacement. Free vibration analysis of the plate by tracing the equilibrium path and natural frequencies reveals the occurrence of the 'mode shifting' phenomenon (exchanging of vibration modes) on the fundamental path for thermally loaded plates. In contrast, for mechanically-loaded plates, the existence of 'curve veering' (the tendency of exchanging of vibration mode) is also observed on the fundamental path.

References

Chai, H., 2002. On the post-buckling behavior of bilaterally constrained plates. International Journal of Solids and Structures 39, 2911–2926.

Chen, H., 2004. Nonlinear analysis of post-buckling dynamics and higher order instabilities of flexible structures. Ph.D. dissertation, Duke University, Durham, NC, December 2004.

Chen, H., Virgin, L.N., 2004. Dynamic analysis of modal shifting and mode jumping in thermally buckled plates. Journal of Sound and Vibration 278, 233–256.

Chen, H., Virgin, L.N. Asymptotic and non-stationary finite element analysis of post-buckling dynamics in plates—Part I: Asymptotic analysis. International Journal of Solids and Structures, in press.

Chien, C.-S., Gong, S.-Y., Mei, Z., 2000. Mode jumping in the von Kármán equations. SIAM Journal of Scientific Computing 22, 1354–1385.

Crisfield, M.A., 1997. Non-linear Finite Element Analysis of Solids and Structures, vol. 2. John Wiley & Sons.

Dossou, K., Pierre, R., 2003. A Newton–GMRES approach for the analysis of the postbuckling behavior of the solutions of the von Kármán equations. SIAM Journal of Scientific Computing 24, 1994–2012.

Everall, P.R., Hunt, G.W., 1999. Arnold tongue predictions of secondary buckling in thin elastic plates. Journal of the Mechanics and Physics of Solids 47, 2187–2206.

Falzon, B.G., Steven, G.P., 1997. Buckling mode transition in hat-stiffened composite panels loaded in uniaxial compression. Composite Structures 37, 253–267.

Hobart, K.D., Kub, F.J., Fatemi, M., Twigg, M.E., Thompson, P.E., Kuan, T.S., Inoki, C.K., 2000. Compliant substrates: a comparative study of the relaxation mechanics of strained films bounded to high and low viscosity oxides. Journal of Electronic Materials 29, 897–900.

Huang, R., Suo, Z., 2002. Wrinkling of a compressed elastic film on a viscous layer. Journal of Applied Physics 91, 1135–1142.

Knight, N.F., Starnes Jr., J.H., 1988. Postbuckling behavior of selected curved stiffened graphite-epoxy panels loaded in axial compression. AIAA Journal 26, 344–352.

Marcinowski, J., 1999. Postbuckling behaviour of rectangular plates in axial compression. Archives of Civil Engineering 45, 275–288.

Muheim, D.M., Johnson, E.R., 2003. Mode jumping of an isogrid panel under quasi-static compression. In: Proceedings of 44th AIAA/ASME/ASCE/AHS Structures, Structural Dynamics and Materials Conference, AIAA-2003-1790, vol. 5, Norfolk, VA, April 2003, pp. 3591–3601.

Palasantzas, G., De Hosson, J.M., 2003. Evolution of normal stress and surface roughness in buckled thin films. Journal of Applied Physics 93, 893–897.

Plaut, R.H., Murphy, K.D., Virgin, L.N., 1995. Curve and surface veering for a braced column. Journal of Sound and Vibration 187, 879–885.

Riks, E., Rankin, C.C., 2002. Sandwich modeling with an application to the residual strength analysis of a damaged compression panel. International Journal of Non-Linear Mechanics 37, 897–908.

Riks, E., Rankin, C.C., Brogan, F.A., 1996. On the solution of mode jumping phenomena in thin-walled shell structures. Computer Methods in Applied Mechanics and Engineering 136, 59–92.

Sridhar, N., Srolovitz, D.J., Suo, Z., 2001. Kinetics of buckling of compressed film on a viscous substrate. Applied Physics Letters 78, 2482–2484.

Sridhar, N., Cox, B.N., Srolovitz, D.J., 2003. Mechanism map for a misfitting film on a viscous substrate. Applied Physics Letters 82, 2233–2235.

Stein, M., 1959. Loads and deformation of buckled rectangular plates. NASA Technical Report R-40, National Aeronautics and Space Administration.

Stoll, F., 1994. Analysis of the snap phenomenon in buckled plates. International Journal of Non-Linear Mechanics 29, 123–138.

Stoll, F., Olson, S.E., 1997. Finite element investigation of the snap phenomenon in buckled plates. In: Proceedings of the 1997 38th AIAA/ASME/ASCE/AHS/ASC Structures, Structural Dynamics, and Materials Conference, vol. 4, pp. 2703–2712.

Supple, W.J., 1968. On the change in buckle pattern in elastic structures. International Journal of Mechanical Sciences 10, 737–745.

Tiwari, N., Hyer, M.W., 2002. Secondary buckling of compression-loaded composite plates. AIAA Journal 40, 2120–2126.

Virgin, L.N., Plaut, R.H., 2002. Use of frequency data to predict secondary bifurcation. Journal of Sound and Vibration 251, 919–926.